



## Early View

Original article

### **Diverse Cardiopulmonary Diseases are Associated with Distinct Xenon MRI Signatures**

Ziyi Wang, Elianna A. Bier, Aparna Swaminathan, Kishan Parikh, John Nouls, Mu He, Joseph G. Mammarrappallil, Sheng Luo, Bastiaan Driehuys, Sudarshan Rajagopal

Please cite this article as: Wang Z, Bier EA, Swaminathan A, *et al.* Diverse Cardiopulmonary Diseases are Associated with Distinct Xenon MRI Signatures. *Eur Respir J* 2019; in press (<https://doi.org/10.1183/13993003.00831-2019>).

This manuscript has recently been accepted for publication in the *European Respiratory Journal*. It is published here in its accepted form prior to copyediting and typesetting by our production team. After these production processes are complete and the authors have approved the resulting proofs, the article will move to the latest issue of the ERJ online.

Copyright ©ERS 2019

# Diverse Cardiopulmonary Diseases are Associated with Distinct Xenon MRI Signatures

Ziyi Wang<sup>1,2\*</sup>, Elianna. A. Bier<sup>1,2\*</sup>, Aparna Swaminathan<sup>3</sup>, Kishan Parikh<sup>3</sup>, John Nouls<sup>4</sup>, Mu He<sup>2,5</sup>, Joseph G. Mammarrappallil<sup>4</sup>, Sheng Luo<sup>6</sup>, Bastiaan Driehuys<sup>1,2,4</sup>, Sudarshan Rajagopal<sup>7</sup>

*\*Denotes equal contributions to first authorship*

<sup>1</sup>*Department of Biomedical Engineering, Duke University, Durham, NC, USA*

<sup>2</sup>*Center for In Vivo Microscopy, Duke University Medical Center, Durham, NC, USA*

<sup>3</sup>*Division of Pulmonary, Allergy, and Critical Care, Department of Medicine, Duke University Medical Center, Durham, NC, USA*

<sup>4</sup>*Department of Radiology, Duke University Medical Center, Durham, NC, USA*

<sup>5</sup>*Department of Electrical and Computer Engineering, Duke University, Durham, NC, USA*

<sup>6</sup>*Department of Biostatistics & Bioinformatics, Duke University Medical Center, Durham, NC, USA*

<sup>7</sup>*Division of Cardiology, Department of Medicine, Duke University Medical Center, Durham, NC, USA*

## Abstract

### Background

As an increasing number of patients exhibit concomitant cardiac and pulmonary disease, limitations of standard diagnostic criteria are more frequently encountered. Here, we apply noninvasive <sup>129</sup>Xenon MR imaging and spectroscopy to identify patterns of regional gas transfer impairment and hemodynamics that are uniquely associated with chronic obstructive pulmonary disease (COPD), idiopathic pulmonary fibrosis (IPF), left heart failure (LHF), and pulmonary arterial hypertension (PAH).

### Methods

Healthy volunteers (n=23) and patients with COPD (n=8), IPF (n=12), LHF (n=6), and PAH (n=10) underwent <sup>129</sup>Xe gas transfer imaging and dynamic spectroscopy. For each patient, 3D maps were generated to depict ventilation, barrier uptake (<sup>129</sup>Xe dissolved in interstitial tissue), and red blood cell (RBC) transfer (<sup>129</sup>Xe dissolved in RBCs). Dynamic <sup>129</sup>Xe spectroscopy was used to quantify cardiogenic oscillations in the RBC signal amplitude and frequency shift.

### Results

Compared to healthy volunteers, all patient groups exhibited decreased ventilation and RBC transfer ( $p \leq 0.01$ ,  $p \leq 0.01$ ). Patients with COPD demonstrated more ventilation and barrier defects compared to all other groups ( $p \leq 0.02$ ,  $p \leq 0.02$ ). In contrast, IPF patients demonstrated elevated barrier uptake compared to all other groups ( $p \leq 0.007$ ) and increased RBC amplitude and shift oscillations compared to healthy volunteers ( $p = 0.007$ ,  $p \leq 0.01$ ). Patients with COPD and PAH both exhibited decreased RBC amplitude oscillations ( $p = 0.02$ ,  $p = 0.005$ ) compared to healthy volunteers. LHF was distinguishable from PAH by enhanced RBC amplitude oscillations ( $p = 0.01$ ).

## Conclusion

COPD, IPF, LHF, and PAH each exhibit unique  $^{129}\text{Xe}$  MR imaging and dynamic spectroscopy signatures. These metrics may help with diagnostic challenges in cardiopulmonary disease and increase understanding of regional lung function and hemodynamics at the alveolar-capillary level.

**Funding:** NIH/NHLBI R01 HL105643, NIH/NHLBI R01HL126771, and HHSN268201700001C

## Introduction

Over the past thirty years, mortality related to both chronic obstructive pulmonary disease (COPD) and interstitial lung disease (ILD), has increased in the United States [1]. Among the factors associated with increased mortality in both COPD and ILD is the frequent presence of comorbid cardiovascular disease such as heart failure (HF) [2, 3]. Acute respiratory symptoms in patients with comorbid HF and lung disease can often have mixed cardiac and pulmonary origins, which complicates the interpretation of standard diagnostic testing [4]. For example, in patients with concomitant COPD and HF, interpretation of spirometry may be challenging [5] and echocardiographic acoustic windows may be impeded by gas trapping [6]. Similarly, pulmonary edema can mimic certain types of ILD on CT scans [7].

MRI has become a valuable tool for evaluation pulmonary hypertension and heart failure, owing to its non-invasive nature, high reproducibility and sensitivity to change in morphological, functional and flow related parameters [8]. Multiparametric cardiac MRI models have high diagnostic accuracy in patients suspected of having pulmonary hypertension [9]. Dynamic contrast-enhanced lung perfusion MRI has high sensitivity compared to scintigraphy in screening for chronic thromboembolic pulmonary hypertension [10] and MRI has been used to predict mean pulmonary artery pressure in patients with COPD [11]. However, these methods do not directly address ventilation and pulmonary gas exchange, nor do they address impairment occurring within the microvasculature.

To address these challenges, MRI using hyperpolarized  $^{129}\text{Xe}$  ( $^{129}\text{Xe}$ ) is emerging as a promising means for non-invasive spatially resolved assessment of pulmonary function [12]. This method, which is rapid and well-tolerated, permits direct 3D imaging, not only of ventilation distribution, but also pulmonary gas transfer. This is enabled by the free diffusion of xenon from the alveoli, through the interstitial barrier tissues (comprised of alveolar epithelial cells, interstitial tissues, capillary endothelial cells, and plasma), and into red blood cells (RBCs) (Figure 1); in each of these 3 compartments  $^{129}\text{Xe}$  exhibits distinct frequency shifts [12]. Thus, with two breath-holds of  $^{129}\text{Xe}$ , quantitative maps can now be generated to depict the distribution of  $^{129}\text{Xe}$  in airspaces, its uptake in barrier tissues and its transfer to RBCs [13, 14]. This imaging approach is now capable of spatially resolving the heterogeneous disease burden for a wide array of conditions, including COPD, idiopathic pulmonary fibrosis (IPF), and pulmonary vascular disease (PVD) [15, 16]. Furthermore, while  $^{129}\text{Xe}$  imaging provides useful quantification of regional functional burden, a more detailed characterization of whole-lung  $^{129}\text{Xe}$  spectroscopic indices provide additional metrics that may help to further discriminate the underlying pathologies. For example, in IPF the spectroscopic ratio of RBC to barrier signal provides a global metric of gas transfer impairment that has been shown to strongly correlate with the diffusing capacity for carbon monoxide ( $\text{DL}_{\text{CO}}$ ) [17]. Moreover, the signal frequency of  $^{129}\text{Xe}$  interacting with capillary RBCs is uniquely sensitive to their level of oxygenation [18]. Such  $^{129}\text{Xe}$  spectra can be acquired dynamically

every 20ms, revealing temporal oscillations in pulmonary gas exchange that reflect cardiopulmonary hemodynamics [19].

The array of non-invasive imaging and spectroscopic markers of pulmonary gas transfer and hemodynamics that can be derived from hyperpolarized  $^{129}\text{Xe}$  presents an appealing approach for comprehensive and non-invasive phenotyping of cardiopulmonary physiology in individual patients. However, to date most studies have focused on only one form of  $^{129}\text{Xe}$  contrast or investigated them in only a single disease. Here, we sought to apply a comprehensive panel of non-invasive  $^{129}\text{Xe}$  MR imaging and spectroscopy to a cohort of patients with known heart and lung disease in order to identify features that could differentiate signatures of COPD, IPF, left heart failure (LHF), or pulmonary arterial hypertension (PAH).

## Methods

### Subject Recruitment

The protocol was approved by the Institutional Review Board of Duke University Medical Center. Healthy volunteers, and patients with a clinical diagnosis of COPD, IPF, LHF, or PAH were recruited, and all provided written, informed consent. All healthy volunteers had no smoking history or known respiratory conditions. COPD was diagnosed using spirometric measures of post-bronchodilator forced expiratory volume in one second ( $\text{FEV}_1$ )/forced vital capacity (FVC)  $\leq 70\%$  predicted [20]. The diagnosis of IPF was established according to ATS/ERS criteria, either from a confirmed pattern of usual interstitial pneumonia (UIP) on CT or from surgical lung biopsy [21]. LHF consisted of patients with both heart failure preserved ejection fraction (HFpEF;  $n=4$ ) or heart failure with reduced ejection fraction (HFrEF;  $n=2$ ), which was confirmed by echocardiogram [22]. The patients with HFpEF had an LVEF  $\geq 55\%$  and either evidence of an elevated pulmonary capillary wedge pressure (PCWP)  $> 15$  mmHg at right heart catheterization ( $n=2$ , PCWP 19 and 38) and/or clinical evidence of left heart failure without echocardiographic or catheterization evidence of precapillary pulmonary hypertension or right heart failure ( $n=4$ ). PAH was defined according to the World Health Organization criteria and diagnosed by right heart catheterization with a resting mean pulmonary arterial pressure (mPAP)  $\geq 25$  mmHg and a PCWP  $\leq 15$  mmHg [23]. Hemodynamics of the PAH group at the time of diagnosis were as follows (median; interquartile range): mPAP (46; 39, 59), PCWP (12; 10,14), PVR (6; 4, 8), cardiac index (2.9; 2.4, 3.5). All clinical tests were performed as a part of routine care. Pulmonary function tests (PFTs) were performed on all patients and 83% of healthy volunteers to assess baseline pulmonary function.

### $^{129}\text{Xe}$ Gas Hyperpolarization and MRI Acquisition

$^{129}\text{Xe}$  gas was hyperpolarized via continuous flow spin exchange optical pumping and cryogenic accumulation [24], using commercially available systems (Model 9820 and 9810, Polarean, Durham, NC).  $^{129}\text{Xe}$  spectroscopy and imaging were acquired on either a 1.5T (GE 15M4 EXCITE) or a 3T (SIEMENS MAGNETOM Trio) scanner during 2 separate breath holds of  $^{129}\text{Xe}$ . Subjects first underwent dynamic spectroscopy during which  $^{129}\text{Xe}$  free induction decays (FIDs) were collected every 20 ms (TE = 0.932ms, flip angle  $\approx 20^\circ$ , dwell time = 32 $\mu\text{s}$ , 512/1024 points) during a breath-hold [19]. 3D images were then acquired using an interleaved radial acquisition of gas- and dissolved-phase signal during a 15 second breath-hold. The signal was acquired at an echo time that allowed the two-dissolved phase

compartments to be decomposed using the 1-point Dixon method [12]. This generated 3D images of the gas, barrier, and RBC components with 2.8 mm isotropic voxels.

### **Quantitative Processing and Analysis**

3D images of each compartment were rendered into quantitative maps and cast into color clusters using thresholds derived from healthy reference cohorts established for both 1.5T and 3T acquisitions [13, 25]. Maps of  $^{129}\text{Xe}$  in the barrier tissues and RBCs were normalized on a voxel-by-voxel basis by dividing by the local ventilation signal. The resulting binning maps depict  $^{129}\text{Xe}$  ventilation, barrier tissue uptake ( $^{129}\text{Xe}$  dissolved in interstitial tissue), and RBC transfer ( $^{129}\text{Xe}$  dissolved in RBCs). Each of these maps were quantified by calculating the percentage of the lung exhibiting signal defects and high signal [13]. The dynamically acquired FIDs were fit in the time domain to determine the gas, barrier, and RBC spectral parameters [19]. The time-dependent cardiogenic oscillations in the RBC amplitude and frequency shift were quantified by their peak-to-peak value relative to the mean [19]. Imaging and spectroscopic findings were compared across all cohorts.

### **Statistical Methods**

Imaging and spectroscopic features were compared between cohorts. All computations were performed using JMP 14 (SAS Institute Inc, Cary, NC). First, a one-way analysis of variance was performed using the non-parametric Kruskal-Wallis test. When a significant difference was detected, the Mann Whitney U-test was further used for pairwise analysis. Statistical significance was concluded when  $p < 0.05$ .

## Results

**Table 1: Demographic and Clinical Characteristics stratified by Condition**

Characteristic	Healthy Volunteers N = 23 <sup>a</sup>	COPD N = 8	IPF N = 12	Left Heart Failure N = 6	PAH <sup>b,c</sup> N = 10
Age (years)	26 (22, 32)	61.5 (57.0, 71.8)	68 (63.3, 71.5)	63.5 (58.0, 69.0)	50 (46.5, 54.0)
Female	5 (22%)	3 (38%)	2 (17%)	2 (33%)	5 (50%)
Nonwhite race	7 (30%)	0 (0%)	0 (0%)	1 (17%)	2 (20%)
Body Mass Index	24.0 (23.3, 27.4)	24.3 (22.5, 26.5)	28.8 (24.7, 33.0)	29.4 (25.1, 32.3)	29.6 (24.9, 33.9)
Current or prior tobacco use	0 (0%)	6 (75%)	8 (67%)	4 (67%)	3 (30%)
Supplemental O <sub>2</sub> at rest	0 (0%)	5 (63%)	4 (33%)	1 (17%)	2 (20%)
6MWD <sup>b</sup> (m)		395 (324, 429), N = 4	461 (369, 515), N = 10	451 (374, 528), N = 2	500 (426, 575)
<b>PFT<sup>d</sup></b>					
FEV <sub>1</sub> (% predicted)	92 (78, 102), N = 19	34 (27, 55)	70 (57, 80)	72 (58, 85), N = 4	83 (63, 94), N = 9
FVC (% predicted)	96 (83, 103), N = 19	79 (63, 91)	63 (50, 76)	75 (57, 95), N = 4	96 (68, 99), N = 9
FEV <sub>1</sub> /FVC (% predicted)	81 (78, 88), N = 19	49 (40, 54), N = 7	48 (43, 63), N = 3	84 (81, 89), N = 3	82 (74, 87), N = 4
TLC (% predicted)	102 (92, 113), N = 18	100 (93, 107), N = 2	11.5 (9, 14)	94 (88, 100), N = 2	95 (86, 107), N = 9
DL <sub>CO</sub> (mL/min/mmHg)	28 (22, 31), N = 17	11 (9, 15)	3.3 (2.9, 3.9)	21 (15, 28)	16 (13, 21)
K <sub>CO</sub> (mL/min/mmHg/L)	5.2 (4.7, 5.8), N=17	2.7 (1.7, 4.0), N = 8		4.7 (2.7, 4.8)	3.9 (3.4, 5.2)

IPF = idiopathic pulmonary fibrosis; COPD = chronic obstructive pulmonary disease; PAH = pulmonary arterial hypertension; 6MWD = 6-minute walk distance; PFT = pulmonary function test; PCWP = pulmonary capillary wedge pressure; PVR = pulmonary vascular resistance; RVSP = right ventricular systolic pressure.

Continuous variables presented as median (interquartile range); categorical variables presented as frequency (proportion)

<sup>a</sup> 13 Healthy subjects were scanned on a 1.5 T MRI system while 10 were scanned at 3T. All IPF were scanned at 1.5T. All COPD, LHF, and PAH were scanned at 3T.

<sup>b</sup> PAH patients were on therapy with a combination of prostacyclin analogues, phosphodiesterase-5 inhibitors or endothelin receptor antagonists.

<sup>c</sup> The PAH cohort consisted of 7 with idiopathic PAH, one associated with HIV, one associated with drugs/toxins, and one associated with connective tissue disease.

<sup>d</sup> Most recent available clinical values presented. PFTs were performed within 6 months of MRI for all subjects. Right heart catheterizations were historical and performed at the time of initial diagnosis.

### Study Cohort

This study included 23 healthy volunteers, 8 patients with COPD, 12 with IPF, 6 with LHF, and 10 with PAH. Subject demographics and PFT results are summarized in Table 1.

3D-isotropic images of  $^{129}\text{Xe}$  in the gas, barrier, and RBC compartments were acquired on 19 healthy volunteers and all patients. Dynamic spectroscopy was acquired on 13 healthy volunteers, 6 patients with COPD, 8 with IPF, 5 with LHF, and 10 with PAH.

### Identifying Disease-specific Imaging-derived Metrics

Representative ventilation and gas transfer maps from subjects in each group are depicted in Figure 2. For each map, the percentages of voxels falling in the defect, low, and high bins are reported. In the healthy volunteer, the majority of the  $^{129}\text{Xe}$  signal in all three compartments fell within  $\pm 1$  standard deviation from the mean of the reference distribution and thus, in the “normal” green color bins. By contrast, the COPD subject exhibited significant defects in all 3 compartments — ventilation, barrier, and RBC, indicated by the red color bins. The IPF subject exhibited relatively normal ventilation, but significant areas of high barrier uptake (purple), accompanied by defects in RBC transfer in the lower lobes. Both the LHF and PAH subjects exhibited slight ventilation defects, relatively normal barrier, but more significant deficits in RBC transfer.

Figure 3 evaluates these imaging features quantitatively across the cohorts, comparing the percentages of ventilation defects, RBC defects, barrier defects and high barrier. Compared to healthy subjects, all patient groups exhibited a larger percentage of defects in ventilation ( $p \leq 0.01$  for all comparisons) and RBC transfer ( $p \leq 0.01$  for all comparisons). The COPD cohort stood out for exhibiting the largest percentages of ventilation defects ( $41.5 \pm 22.6\%$ ,  $p \leq 0.02$  for all comparisons) and was the only one to show defects in barrier uptake ( $10.4 \pm 7.1\%$ ,  $p \leq 0.02$  for all comparisons). By contrast, IPF patients were distinguished from the other groups by the largest percentage of voxels with high  $^{129}\text{Xe}$  uptake in the barrier tissue ( $39.8\%$ ,  $p \leq 0.007$  for all comparisons). IPF subjects exhibited only modest ventilation defects ( $11.5 \pm 6.7\%$ ,  $p = 0.0003$  vs healthy) but substantial RBC defects ( $11.3 \pm 6.7\%$ ,  $p = 0.0001$  vs healthy). LHF and PAH patients presented with similar imaging characteristics with mildly elevated ventilation defects (LHF:  $11.7 \pm 6.2\%$ ,  $p = 0.01$  vs healthy; PAH:  $8.4 \pm 4.7\%$ ,  $p = 0.01$  vs healthy) and increased RBC transfer defects (LHF:  $13.3 \pm 10.2\%$ ,  $p = 0.01$  vs healthy; PAH:  $14.5 \pm 9.3\%$ ,  $p = 0.002$  vs healthy).

### Disease-specific Spectroscopy-derived Metrics

Figure 4 shows the RBC signal amplitude and shift oscillations for representative subjects from each group. Notably, the RBC signal amplitudes for each patient oscillate at a frequency identical to the heart rate. The IPF patient also exhibits such cardiogenic oscillations prominently in the RBC frequency shift.

Figure 5 shows the group-wise comparison of the cardiogenic RBC amplitude and shift metrics. In healthy subjects, the RBC amplitudes oscillated at a height of  $10.0 \pm 2.6\%$  peak-to-peak with very little RBC shift oscillation ( $0.07 \pm 0.05$  ppm). The RBC shift only oscillates significantly in the IPF cohort ( $0.46 \pm 0.33$  ppm,  $p \leq 0.01$  for all comparisons). IPF patients also exhibited larger RBC amplitude oscillations ( $16.7 \pm 5.5\%$ ,  $p = 0.007$ ) compared to healthy volunteers. RBC amplitude oscillations were diminished in both COPD and PAH compared to healthy volunteers (COPD:  $5.5 \pm 4.7\%$ ,  $p = 0.02$ ; PAH:  $6.0 \pm 3.6\%$ ,  $p = 0.005$ ). In subjects with LHF, the RBC amplitude oscillations were larger than in healthy volunteers, but this did not reach statistical significance ( $13.0 \pm 5.1\%$ ,  $p = 0.2$ ). However, these oscillations were significantly higher compared to subjects with PAH ( $p = 0.01$ ).

## Discussion

In this study, we identified unique  $^{129}\text{Xe}$  MR imaging and spectroscopy signatures for patients with COPD, IPF, PAH, and LHF. COPD was characterized by significantly elevated ventilation and barrier defect percentages compared to all other disorders, as well as diminished RBC amplitude oscillations. However, in the COPD cohort the ventilation defect percentage varied widely in both scale and distribution, consistent with the heterogeneity of the disease [26]. In contrast, IPF was characterized primarily by elevated barrier uptake, virtually absent barrier defect percentage, elevated RBC amplitude oscillations, and prominent oscillations in RBC shift. PAH and LHF presented with similar imaging characteristics (slight elevations in ventilation, barrier, and RBC defect percentages compared to healthy volunteers). However, PAH was distinguished from LHF by RBC amplitude oscillations that were lower than in healthy subjects, whereas in LHF such oscillations were enhanced. All four disease cohorts exhibited increased RBC transfer defects compared to healthy subjects.

The observation that ventilation defects are prominent in patients with COPD is consistent with numerous previous studies [14, 27, 28]. We now add the observation that, in COPD, barrier uptake is also diminished, likely reflecting emphysematous lung destruction and loss of surface area for gas exchange. This loss would further lead to diminished RBC transfer. In IPF we confirm that the disease is characterized by increased barrier uptake with defects in RBC transfer primarily in the lung bases [14]. Furthermore, we provide important context for our prior work showing that cardiogenic oscillations in  $^{129}\text{Xe}$  RBC amplitude and shift are significantly enhanced in patients with IPF relative to healthy controls [19]. Having now acquired such data in this broader cohort suggests that the RBC shift oscillations are, thus far, unique to IPF, and are not observed COPD, LHF, and PAH. Moreover, the enhanced RBC amplitude oscillations seen in IPF are only additionally seen in LHF, suggesting that perhaps this is a marker of post-capillary PH.

### Connecting $^{129}\text{Xe}$ MRI to conventional metrics of gas exchange

The ability of  $^{129}\text{Xe}$  MRI to produce 3D quantitative maps of ventilation, barrier uptake and RBC transfer invites an effort to relate these imaging features to diffusing capacity ( $DL_{CO}$ ) and its underlying rate constant  $K_{CO}$  ( $DL_{CO}$  divided by accessible alveolar volume  $V_A$ ). This appeals to the framework of Roughton and Forster [29], which treats the diffusing capacity  $D_L$  as being comprised of two serial conductances,

$$\frac{1}{D_L} = \frac{1}{D_M} + \frac{1}{\theta V_C}$$

where  $D_M$  is the membrane conductance, and  $\theta V_C$  is attributable to the capillary blood volume  $V_C$ , and its reaction rate  $\theta$  with CO. The membrane term,  $D_M$ , is directly proportional to the alveolar surface area available for gas exchange, but inversely proportional to barrier thickness. Both these aspects are inherently seen in the  $^{129}\text{Xe}$  barrier/gas signal distribution. When mean barrier/gas ( $\bar{Bar}$ ) decreases, it indicates a loss of surface area, and when it increases, it indicates barrier thickening. This suggests that a patient's  $\bar{Bar}$  compared to a healthy reference value,  $\widetilde{\bar{Bar}} = \bar{Bar}/\bar{Bar}_{ref}$  (or its inverse when  $\bar{Bar} > \bar{Bar}_{ref}$ ) can serve as a surrogate for  $D_M$ .  $\widetilde{\bar{Bar}}$ , constructed in this fashion, is akin to a relative rate constant, and we thus multiply by  $V_A$  and a proportionality constant  $\alpha$  to arrive at the membrane conductance  $D_M = \alpha \widetilde{\bar{Bar}} V_A$ . In a similar manner, mean RBC/gas signal relative to reference, reflects the capillary blood volume conductance according to  $\theta V_C = \beta \widetilde{RBC} V_A$ . Thus, with knowledge of  $\alpha$  and  $\beta$  overall diffusing capacity can be calculated from these xenon MRI metrics as

$$\frac{V_A}{DL_{CO}} = \frac{1}{K_{CO}} = \frac{1}{\alpha \bar{B}ar} + \frac{1}{\beta \overline{RBC}}$$

Notably, the left-hand side of the equation is simply the inverse of the transfer coefficient  $K_{CO}$ . Combined with alveolar volume  $V_A$ , it is also possible to estimate  $DL_{CO}$ . Using the  $^{129}\text{Xe}$  MRI metrics from this full patient cohort, the relevant reference population values [13, 30] and  $K_{CO}$  data, we found  $\alpha=11.0$  and  $\beta=12.8$  mL/min/mmHg/L provided a best fit. This is represented in Figure 6A, showing 3-dimensional surface that reflects the way in which relative barrier and RBC contribute to  $K_{CO}$ . Similarly, the correlation of the image-estimated  $K_{CO}$  and  $DL_{CO}$  values with the measured ones are shown in Figure 6B and C. Within this framework we see that imaging predictions of  $K_{CO}$  are relatively strong and when multiplied by  $V_A$  generates an image-predicted  $DL_{CO}$  that is remarkably well-correlated with the measured value. This approach, which will need to be confirmed prospectively, provides a strong foundation for using  $^{129}\text{Xe}$  MRI to interpret  $DL_{CO}$  across a range of patient populations with all combinations of low and high barrier and as well as capillary blood volumes.

### Alveolar-capillary interface models depicting disease phenotypes

To aid in interpreting the patterns of  $^{129}\text{Xe}$  MRI and spectroscopic signatures of each disease in the context of gas transfer physiology, we propose the following conceptual alveolar-capillary interface architecture (Figure 7). In a healthy subject,  $^{129}\text{Xe}$  atoms freely diffuse into the alveoli and into the alveolar-capillary interface, translating into images reflecting a normal range of ventilation, barrier uptake and RBC transfer. In COPD, chronic airway inflammation and small airway obstruction [31] create ventilation defects, while the loss of alveolar surface area associated with emphysema results in diminished uptake of  $^{129}\text{Xe}$  in the interstitial barrier tissues. This drives a concomitant decrease in RBC transfer, consistent with the low  $DL_{CO}$  values observed in this cohort. However, we note that many patients exhibit disproportionately worse RBC transfer that may reflect an additional loss of vasculature [32]. By contrast, in IPF, interstitial fibrosis creates a larger reservoir for  $^{129}\text{Xe}$  uptake, thus enhancing the barrier signal [33] and in conjunction with regions of RBC transfer defects, reduces  $DL_{CO}$  [15]. It is less clear what causes the defects in RBC transfer in LHF, but it is known that these patients can develop gas exchange abnormalities including a reduction in  $DL_{CO}$  that is thought to be secondary to chronic damage resulting from pulmonary venous congestion [34, 35]. Finally, PAH is characterized by increased pre-capillary impedance, resulting from remodeling and obliteration of the pulmonary arterioles. This results in a loss of alveolar membrane diffusing capacity and pulmonary capillary blood volume as reflected in Figure 7.

RBC amplitude oscillations reflect changes in  $^{129}\text{Xe}$  transfer driven by differences in capillary blood volume during the cardiac cycle. These, in turn, are driven by the right ventricular stroke volume, driving flow through the pre- and post-capillary impedances. In IPF, for example, the stroke volume is delivered to a partially destroyed capillary bed [15]. If stroke volume is preserved, it will produce larger relative capillary blood volume oscillations between systole and diastole, thereby provoking larger RBC amplitude oscillations. Such enhancement is also seen in pulmonary venous hypertension caused by left-sided heart failure. In these patients, enhanced cardiogenic RBC oscillations are consistent with diastolic reserve limitation during the cardiac cycle [36], caused by a high post-capillary impedance. This results in a relative increase in pulmonary capillary blood volume, as RV output transiently exceeds LV output that leads to blood pooling in the pulmonary circulation [34]. In PAH, while capillary blood volume is also reduced [37], the larger impedance to flow in the arterioles causes RBC oscillations to be reduced. It is these amplitude oscillations that appear to be the feature that most strongly differentiates pre-capillary

from post-capillary PH. It is possible that this could be even more clearly demonstrated by correcting the RBC oscillation amplitude for patient-specific stroke volume and capillary bed volume. Thus, future studies could benefit from the addition of cardiac MRI to determine stroke volume and allow for such refinement.

Unique to the IPF patients in this cohort is the observation that the RBC resonant frequency also exhibits cardiogenic oscillations. As the  $^{129}\text{Xe}$ -RBC frequency is strongly dependent on blood oxygenation level [18], we hypothesize that this indicates variability in the blood oxygenation. In IPF subjects, diffusion impairment likely causes large excursions in blood oxygenation as the capillary blood volume is replaced over the course of the cardiac cycle. This likely explains why the RBC frequency shift oscillates cardiogenically in conditions where blood oxygenation is diffusively impaired [19]. Such oscillations are not observed in COPD where gas exchange impairment results from loss of membrane surface area rather than membrane conductance. We should note that all the above interpretations and proposed models will require confirmation in both *in vitro* systems and *in vivo* animal models where each condition can be carefully controlled.

### **Potential for Differentiating Cardiopulmonary Diseases in the Clinical Setting**

Taken together, this combination of non-invasive  $^{129}\text{Xe}$  MR imaging and spectroscopic parameters enables interrogation of gas transfer at the alveolar capillary level that appears useful, not only to characterize disease burden, but also to identify signatures that may ultimately help differentiate cardiopulmonary disorders. A potential approach to such differentiation is seen in Figure 8, which shows radar plots of the 4 key imaging features and 2 key spectroscopic features – ventilation defect, barrier defect, high barrier uptake, RBC defects, and RBC amplitude and shift oscillations. Integrating these features for each disease group provides an initial means of displaying these phenotypes in a visually distinct way. Generating such plots for individual patients could provide a powerful means to identify the primary phenotypes that should be considered.

While our study benefited from using well-characterized patient cohorts, work in patients with mixed cardiopulmonary disease may demonstrate the utility of  $^{129}\text{Xe}$  MRI to determine the underlying cause of dyspnea in patients with concomitant diseases. Furthermore, as early diagnosis is increasingly emphasized in disorders such as ILD [38] and PAH [39],  $^{129}\text{Xe}$  spectroscopic indices may provide a sensitive probe for this as well as allowing for non-invasive tracking of disease progression. Importantly, the RBC transfer signal depicts the ultimate disease burden for gas transfer function, and therefore might be used to evaluate disease progression and therapeutic response [40]. Given the limitations of current diagnostic testing, the information provided by  $^{129}\text{Xe}$  gas transfer imaging and dynamic spectroscopy has the potential to improve patient care.

### **Study limitations and future directions**

We must acknowledge several limitations to this first study comparing  $^{129}\text{Xe}$  MR imaging and spectroscopic signatures across cardiopulmonary conditions. First, the heterogeneity and possible comorbidities of patients in each disease cohort may have limited our ability to identify patterns in  $^{129}\text{Xe}$  imaging and spectroscopy. For example, all PAH patients were undergoing clinically indicated, targeted treatment, which may have limited the severity of their PAH at the time of the  $^{129}\text{Xe}$  study. Because many did not have a recent right heart catheterization available, the severity of their disease could not be assessed at the time of their study. Furthermore, while our study aimed to recruit patients with

isolated LHF as a model for post-capillary impedance, several may have also had right heart failure given the common pathogenic evolution from left heart dysfunction to right heart dysfunction over time [41]. In fact, this phenotypic evolution may partly explain the large variation in RBC amplitude oscillation exhibited by our LHF cohort (Max: 21.5%, Min: 8.0%, SD: 5.1%). Additionally, IPF and COPD subjects were not specifically evaluated to rule out PH. Another limitation is that our subject scans were conducted at different platforms with two field strengths [13, 30]. Our quantification method, using a healthy reference group constructed under the same acquisition protocol, was designed to incorporate the potential factors such as  $T_1$  and  $T_2^*$  decay, which may affect the gas transfer measurements. However, these and other factors constrained the size and gender ratio of the healthy reference cohorts, which were also significantly younger than the typical patients in our cohorts and predominantly male. Since the aging lung is reported to undergo physiological changes that could impact gas transfer functions [42], future studies will benefit from constructing a larger and age-controlled healthy population.

## Conclusions

In this study, we applied  $^{129}\text{Xe}$  gas transfer imaging and spectroscopy on healthy subjects and patients with COPD, IPF, LHF, and PAH. As a non-invasive and non-ionizing tool, hyperpolarized  $^{129}\text{Xe}$  gas transfer MRI provides a fundamentally new approach to directly image regional function while also capturing hemodynamics at the alveolar-capillary level. We identified unique imaging and spectroscopic signatures for each of these diseases, that may help overcome some of the diagnostic challenges faced by clinicians treating patients with cardiopulmonary disease.  $^{129}\text{Xe}$  gas transfer imaging and spectroscopy is a promising technology in characterizing cardiopulmonary disease pathophysiology and with further validation in larger studies, can contribute to a comprehensive understanding of the multifactorial pathogenesis of dyspnea and developing personalized treatment approaches.

## Acknowledgements

We gratefully acknowledge the selfless contributions of our patients and the tireless commitment of our clinical research coordinators Karla Kennedy, Susana Almeida-Peters, Jennifer Korzekwinski and Samantha Womack. Sheng Luo's research was supported in part by National Institutes of Health (grant no: R01NS091307, R56AG062302).

## References

1. Dwyer-Lindgren, L., et al., *Trends and Patterns of Differences in Chronic Respiratory Disease Mortality Among US Counties, 1980-2014*. *Jama*, 2017. **318**(12): p. 1136-1149.
2. Divo, M., et al., *Comorbidities and Risk of Mortality in Patients with Chronic Obstructive Pulmonary Disease*. *American Journal of Respiratory and Critical Care Medicine*, 2012. **186**(2): p. 155-161.
3. Kreuter, M., et al., *Impact of Comorbidities on Mortality in Patients with Idiopathic Pulmonary Fibrosis*. *PLoS One*, 2016. **11**(3): p. e0151425.
4. Roversi, S., et al., *Chronic Obstructive Pulmonary Disease and Cardiac Diseases. An Urgent Need for Integrated Care*. 2016. **194**(11): p. 1319-1336.
5. Minasian, A.G., et al., *Serial pulmonary function tests to diagnose COPD in chronic heart failure*. *Transl Respir Med*, 2014. **2**(1): p. 12.

6. Hawkins, N.M., S. Virani, and C. Ceconi, *Heart failure and chronic obstructive pulmonary disease: the challenges facing physicians and health services*. Eur Heart J, 2013. **34**(36): p. 2795-803.
7. Storto, M.L., et al., *Hydrostatic pulmonary edema: high-resolution CT findings*. AJR Am J Roentgenol, 1995. **165**(4): p. 817-20.
8. Swift, A.J., et al., *Quantitative Magnetic Resonance Imaging of Pulmonary Hypertension A Practical Approach to the Current State of the Art*. Journal of Thoracic Imaging, 2014. **29**(2): p. 68-79.
9. Johns, C.S., et al., *Diagnosis of Pulmonary Hypertension with Cardiac MRI: Derivation and Validation of Regression Models*. Radiology, 2019. **290**(1): p. 61-68.
10. Johns, C.S., et al., *Lung Perfusion: MRI vs. SPECT for Screening in Suspected Chronic Thromboembolic Pulmonary Hypertension*. Journal of Magnetic Resonance Imaging, 2017. **46**(6): p. 1693-1697.
11. Johns, C.S., et al., *Non-invasive methods for estimating mPAP in COPD using cardiovascular magnetic resonance imaging*. European Radiology, 2018. **28**(4): p. 1438-1448.
12. Kaushik, S.S., et al., *Single-breath clinical imaging of hyperpolarized ( $^{129}\text{Xe}$ ) in the airspaces, barrier, and red blood cells using an interleaved 3D radial 1-point Dixon acquisition*. Magn Reson Med, 2016. **75**(4): p. 1434-43.
13. Wang, Z., et al., *Quantitative analysis of hyperpolarized  $^{129}\text{Xe}$  gas transfer MRI*. Med Phys, 2017. **44**(6): p. 2415-2428.
14. Wang, Z., et al., *Hyperpolarized ( $^{129}\text{Xe}$ ) gas transfer MRI: the transition from 1.5T to 3T*. Magn Reson Med, 2018.
15. Wang, J.M., et al., *Using hyperpolarized ( $^{129}\text{Xe}$ ) MRI to quantify regional gas transfer in idiopathic pulmonary fibrosis*. Thorax, 2018. **73**(1): p. 21-28.
16. Dahhan, T., et al., *Abnormalities in hyperpolarized ( $^{129}\text{Xe}$ ) magnetic resonance imaging and spectroscopy in two patients with pulmonary vascular disease*. Pulm Circ, 2016. **6**(1): p. 126-31.
17. Weatherley, N.D., et al., *Hyperpolarised xenon magnetic resonance spectroscopy for the longitudinal assessment of changes in gas diffusion in IPF*. Thorax, 2018.
18. Norquay, G., et al., *Xe-129 Chemical Shift in Human Blood and Pulmonary Blood Oxygenation Measurement in Humans Using Hyperpolarized Xe-129 NMR*. Magnetic Resonance in Medicine, 2017. **77**(4): p. 1399-1408.
19. Bier, E.A., et al., *A protocol for quantifying cardiogenic oscillations in dynamic ( $^{129}\text{Xe}$ ) gas exchange spectroscopy: The effects of idiopathic pulmonary fibrosis*. NMR Biomed, 2018: p. e4029.
20. Celli, B.R., W. MacNee, and A.E.T. Force, *Standards for the diagnosis and treatment of patients with COPD: a summary of the ATS/ERS position paper*. Eur Respir J, 2004. **23**(6): p. 932-46.
21. Raghu, G., et al., *An official ATS/ERS/JRS/ALAT statement: idiopathic pulmonary fibrosis: evidence-based guidelines for diagnosis and management*. Am J Respir Crit Care Med, 2011. **183**(6): p. 788-824.
22. Lang, *Recommendations for Cardiac Chamber Quantification by Echocardiography in Adults: An Update from the American Society of Echocardiography and the European Association of Cardiovascular Imaging (vol 28, pg 1, 2015)*. Journal of the American Society of Echocardiography, 2016. **29**(6): p. 521-521.
23. Simonneau, G., et al., *Updated Clinical Classification of Pulmonary Hypertension*. Journal of the American College of Cardiology, 2009. **54**(1): p. S43-S54.
24. Roos, J.E., et al., *Hyperpolarized Gas MR Imaging: Technique and Applications*. Magn Reson Imaging Clin N Am, 2015. **23**(2): p. 217-29.
25. He, M., et al., *Using Hyperpolarized  $^{129}\text{Xe}$  MRI to Quantify the Pulmonary Ventilation Distribution*. Acad Radiol, 2016. **23**(12): p. 1521-1531.

26. Pike, D., et al., *Regional Heterogeneity of Chronic Obstructive Pulmonary Disease Phenotypes: Pulmonary He-3 Magnetic Resonance Imaging and Computed Tomography*. *Copd-Journal of Chronic Obstructive Pulmonary Disease*, 2016. **13**(5): p. 601-609.
27. Qing, K., et al., *Assessment of lung function in asthma and COPD using hyperpolarized 129Xe chemical shift saturation recovery spectroscopy and dissolved-phase MRI*. *NMR Biomed*, 2014. **27**(12): p. 1490-501.
28. Virgincar, R.S., et al., *Quantitative analysis of hyperpolarized 129Xe ventilation imaging in healthy volunteers and subjects with chronic obstructive pulmonary disease*. *NMR Biomed*, 2013. **26**(4): p. 424-35.
29. Roughton, F.J. and R.E. Forster, *Relative importance of diffusion and chemical reaction rates in determining rate of exchange of gases in the human lung, with special reference to true diffusing capacity of pulmonary membrane and volume of blood in the lung capillaries*. *J Appl Physiol*, 1957. **11**(2): p. 290-302.
30. Wang, Z., et al. *Quantifying Hyperpolarized 129Xe Gas Exchange MRI Across Platforms, Field Strength, and Acquisition Parameters* in *Proc. Intl. Soc. Mag. Reson. Med.* 2019. Montreal, QC.
31. Barnes, P.J. and B.R. Celli, *Systemic manifestations and comorbidities of COPD*. *European Respiratory Journal*, 2009. **33**(5): p. 1165-1185.
32. Rahaghi, F.N., E.J.R. van Beek, and G.R. Washko, *Cardiopulmonary Coupling in Chronic Obstructive Pulmonary Disease The Role of Imaging*. *Journal of Thoracic Imaging*, 2014. **29**(2): p. 80-91.
33. Lederer, D.J. and F.J. Martinez, *Idiopathic Pulmonary Fibrosis*. *N Engl J Med*, 2018. **379**(8): p. 797-798.
34. Olson, T.P., B.D. Johnson, and B.A. Borlaug, *Impaired Pulmonary Diffusion in Heart Failure With Preserved Ejection Fraction*. *Jacc-Heart Failure*, 2016. **4**(6): p. 490-498.
35. Guazzi, M., *Alveolar Gas Diffusion Abnormalities in Heart Failure*. *Journal of Cardiac Failure*, 2008. **14**(8): p. 695-702.
36. Borlaug, B.A., et al., *Diastolic relaxation and compliance reserve during dynamic exercise in heart failure with preserved ejection fraction*. *Heart*, 2011. **97**(12): p. 964-9.
37. Farha, S., et al., *Loss of alveolar membrane diffusing capacity and pulmonary capillary blood volume in pulmonary arterial hypertension*. *Respir Res*, 2013. **14**: p. 6.
38. Cosgrove, G.P., et al., *Barriers to timely diagnosis of interstitial lung disease in the real world: the INTENSITY survey*. *BMC Pulm Med*, 2018. **18**(1): p. 9.
39. Lau, E.M., M. Humbert, and D.S. Celermajer, *Early detection of pulmonary arterial hypertension*. *Nat Rev Cardiol*, 2015. **12**(3): p. 143-55.
40. Mammarrappallil, J.G., et al., *New Developments in Imaging Idiopathic Pulmonary Fibrosis With Hyperpolarized Xenon Magnetic Resonance Imaging*. *J Thorac Imaging*, 2019. **34**(2): p. 136-150.
41. Rosenkranz, S., et al., *Left ventricular heart failure and pulmonary hypertension*. *Eur Heart J*, 2016. **37**(12): p. 942-54.
42. Janssens, J.P., J.C. Pache, and L.P. Nicod, *Physiological changes in respiratory function associated with ageing*. *Eur Respir J*, 1999. **13**(1): p. 197-205.

## Figure Captions

Figure 1. (A)  $^{129}\text{Xe}$  freely diffuses from airspace to interstitial barrier tissues to RBCs. In these compartments, the  $^{129}\text{Xe}$  atom exhibits distinct frequency shifts of 0 ppm, 198 ppm, and 217 ppm, respectively. (B) These properties are exploited to enable 3D imaging and quantification of  $^{129}\text{Xe}$  distribution in airspace (ventilation), its barrier uptake and RBC transfer. These maps are color coded to represent different signal intensity levels with the central green bins representing voxels in the normal reference range. (C)  $^{129}\text{Xe}$  spectra are acquired dynamically every 20ms, revealing cardiogenic oscillations of RBC amplitude (%) and frequency shift (ppm).

Figure 2. Ventilation, and normalized barrier uptake, and RBC transfer maps of representative subjects from each cohort. The color bins represent signal intensity, with red for the lowest and blue/purple for the highest and green representing voxels in the healthy reference range. Each map is quantified by the percentage of defect (D), low (L), and high (H), calculated respectively as the voxel fraction of the lowest, second lowest, and the highest two bins for each map. The voxels with ventilation defect were excluded from the analysis of barrier uptake and RBC transfer maps.

Figure 3. Ventilation defect, RBC defect, Barrier defect and Barrier high percentage comparisons for all cohorts. Asterisks indicate a significantly increased (red) or decreased (green) value compared to all other cohorts. Compared to healthy subjects, all disease cohorts showed increased ventilation defect ( $p \leq 0.01$ ) and RBC defect ( $p \leq 0.01$ ). COPD was characterized by significantly elevated percentages of ventilation defects ( $p \leq 0.02$ ) and barrier defects ( $p \leq 0.02$ ). IPF uniquely exhibited reduced barrier defects ( $p \leq 0.02$ ) but elevated percentages of high barrier ( $p \leq 0.007$ ). PAH and LHF exhibited slightly elevated ventilation defects and modestly elevated RBC defects.

Figure 4. RBC signal amplitude and frequency shift demonstrate cardiogenic oscillations in representative patients. Both the IPF and LHF patient exhibit enhanced RBC amplitude oscillations. By contrast, RBC signal oscillations are diminished in both the PAH and COPD patients. Only the IPF patient exhibits oscillations in the RBC shift.

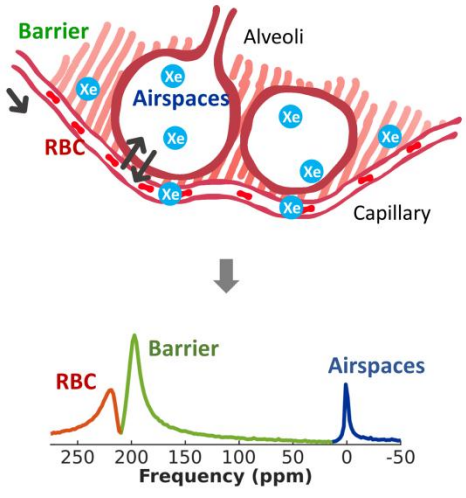
Figure 5. RBC amplitude and frequency shift oscillations compared across cohorts. Gray asterisks mark a significant difference between cohorts and red asterisk marks increased value compared to all other cohorts. Compared to healthy subjects, COPD ( $p = 0.02$ ) and PAH ( $p = 0.005$ ) exhibited decreased RBC amplitude oscillations, while they were increased in IPF ( $p = 0.007$ ). Moreover, in LHF the RBC amplitude oscillations were significantly increased compared to PAH ( $p = 0.01$ ). IPF patients exhibited significantly increased RBC shift oscillations compared to all other cohorts ( $p \leq 0.01$ ).

Figure 6. (A) 3-dimensional surface plot reflects relative contribution of barrier and RBC to  $K_{\text{CO}}$ . (B) The image-estimated  $K_{\text{CO}}$  shows strong correlation with measured  $K_{\text{CO}}$ . (C) This estimated  $K_{\text{CO}}$ , when combined with measured  $V_A$ , produces an estimated  $DL_{\text{CO}}$  which shows an even stronger correlation with the measured  $DL_{\text{CO}}$  values.

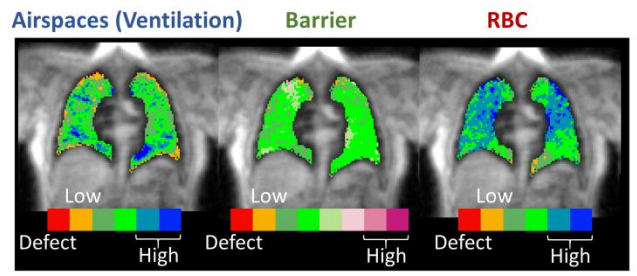
Figure 7. Conceptual architectures of the alveolar-capillary interface to aid in interpreting the  $^{129}\text{Xe}$  imaging and spectroscopic biomarkers across disease states. The diagrams illustrate the alveoli, capillary blood vessel, interstitial barrier tissues, RBCs, and  $^{129}\text{Xe}$  atoms. For each disease state the anticipated effect on the  $^{129}\text{Xe}$  biomarker is shown.

Figure 8. Radar plots to display the primary  $^{129}\text{Xe}$  MR imaging and spectroscopic signatures associated with patients with COPD, IPF, LHF, and PAH. Here the mean cohort values of the key markers are plotted on one of the 6 radials - ventilation defect, barrier defect, barrier high, RBC defect percentages derived from imaging, and RBC shift oscillation and amplitude oscillation from spectroscopy.

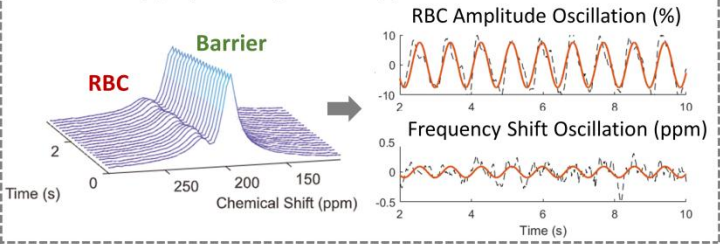
(A) Alveolus-Capillary Model and  $^{129}\text{Xe}$  spectrum

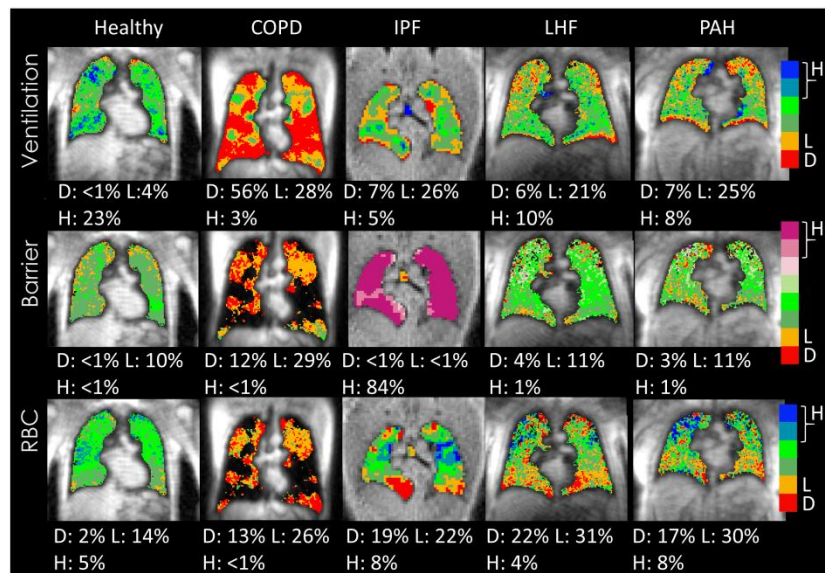


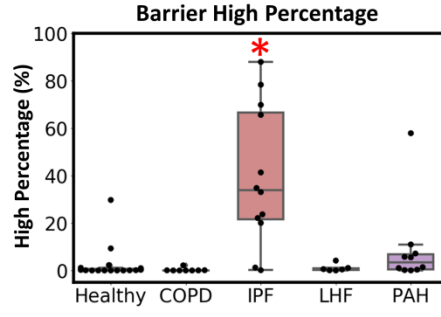
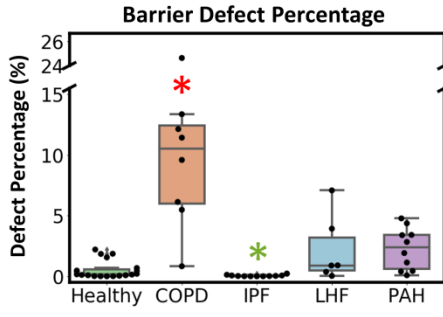
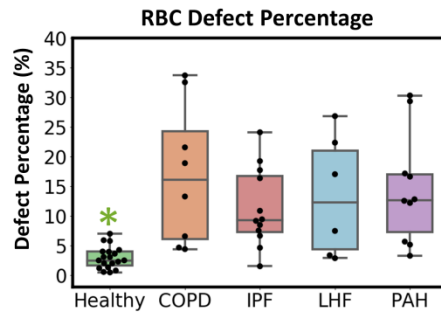
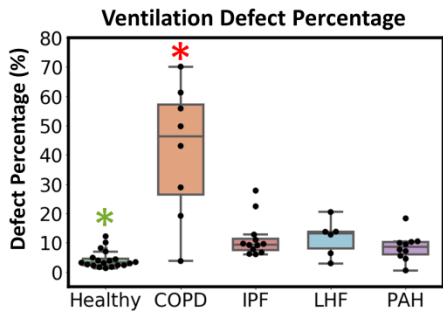
(B) 3D Imaging and Quantification

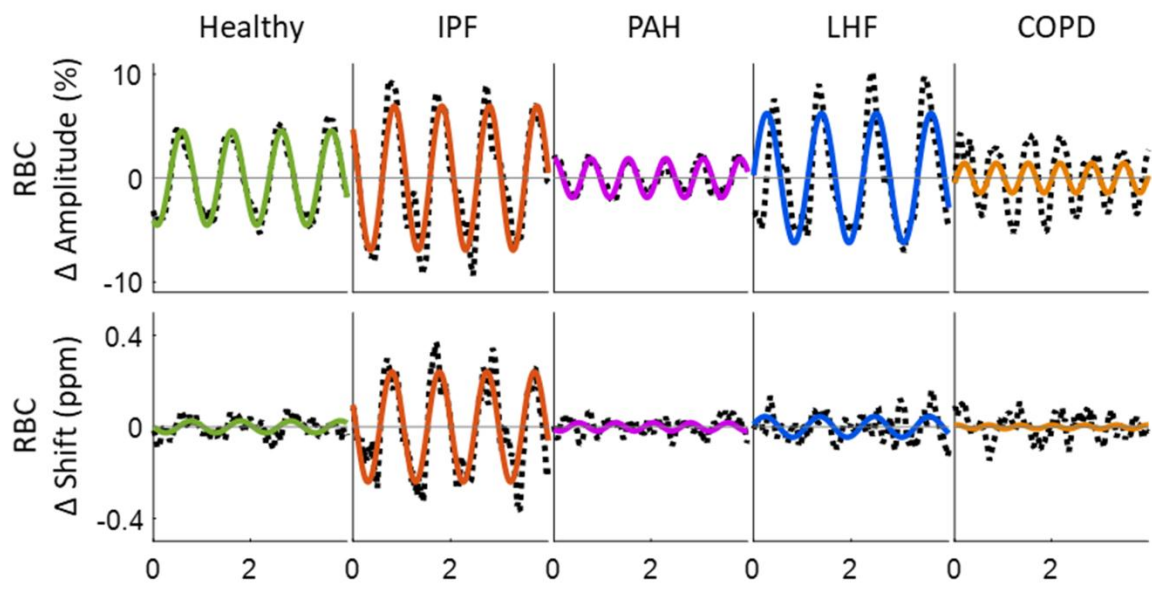


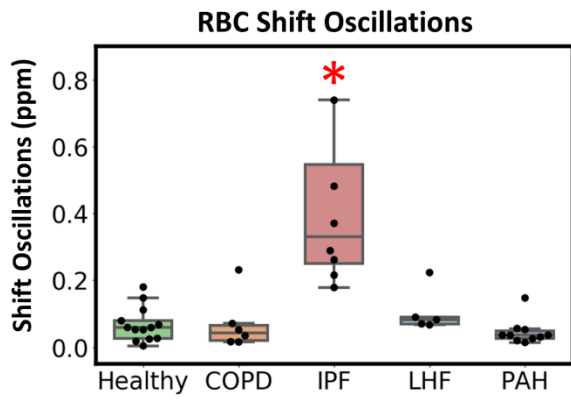
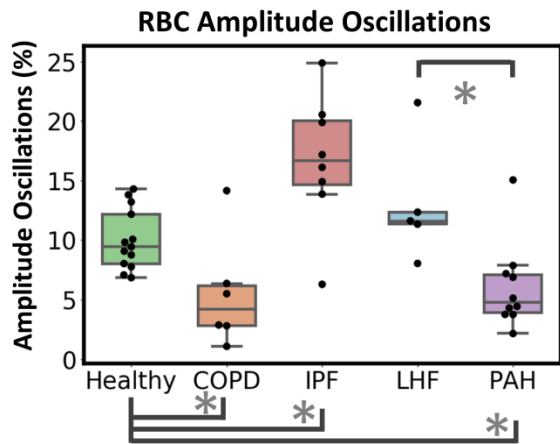
(C) Dynamic Spectroscopy and Quantification



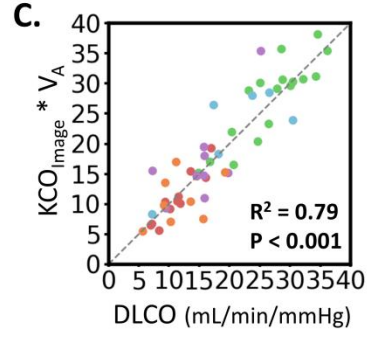
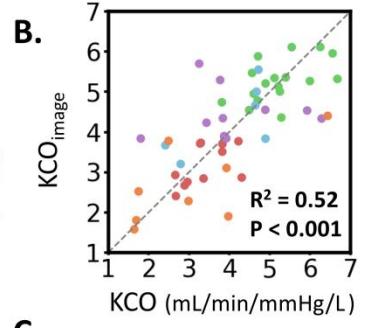
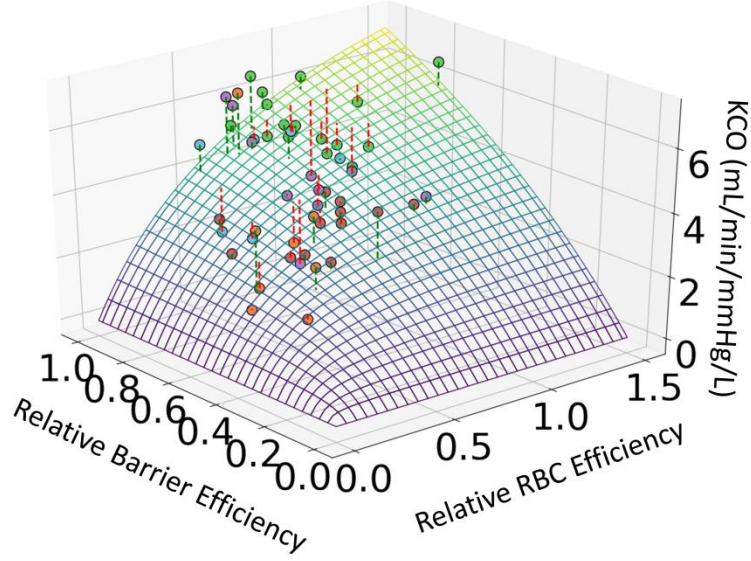




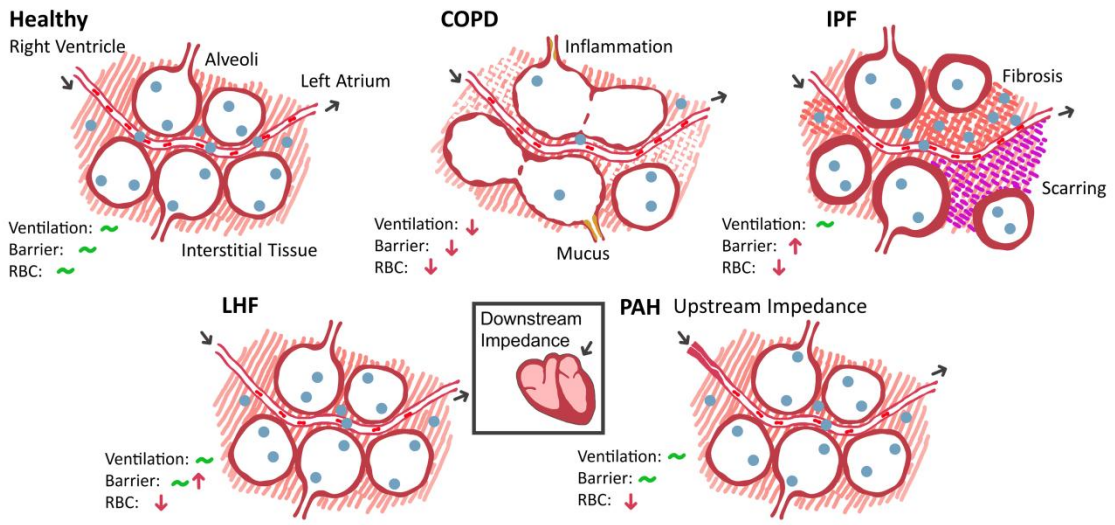




**A.** ● Healthy ● COPD ● IPF ● LHF ● PAH



## Conceptual Architecture of the Alveolar-Capillary Interface



**<sup>129</sup>Xe MR Imaging and Spectroscopy Signatures**

